

ARTICLE OPEN



Part II model support on a new mechanism for North Pacific Oscillation influence on ENSO

Jiuwei Zhao^{1,2}, Mi-Kyung Sung^{3✉}, Jae-Heung Park^{1,2}, Jing-Jia Luo¹ and Jong-Seong Kug^{1,2,4✉}

Owing to the significant influence of El Niño–Southern Oscillation (ENSO) on global climate, how ENSO events are initiated is an intriguing issue. The North Pacific Oscillation (NPO), a primary atmospheric variability over the midlatitude, is a well-known trigger for ENSO events, but the physical linkage is not yet fully understood. Based on observational analyses, in Part I, we proposed a new mechanism that the NPO-related wave activity flux (WAF) could directly induce the equatorial wind anomalies in both upper and lower levels. In this study, we substantiate the impacts of the WAF on tropical circulations using climate models participating in the Coupled Model Intercomparison Project phases 5 and 6 (CMIP5/6). We found that the intensity of the southward WAF over the central Pacific is a paramount factor resulting in intermodel diversity in simulating the NPO–ENSO linkage. By classifying the models into two groups of strong and weak meridional WAF (MWAF), we reveal that the strong MWAF models simulate stronger upper- and lower-level equatorial winds and precipitation anomalies that facilitate the ENSO in subsequent winter. We also reveal that the magnitude of the MWAF is closely related to the model's climatological meridional wind and meridional shear of climatological zonal wind, emphasizing the role of systematic bias on the ENSO simulation. A comparison of the MWAF impact and seasonal footprinting mechanism demonstrates the dominant influence of the MWAF in determining the diversity of NPO–ENSO relationships.

npj Climate and Atmospheric Science (2023)6:16; <https://doi.org/10.1038/s41612-023-00337-y>

INTRODUCTION

The El Niño–Southern Oscillation (ENSO) is a dominant atmosphere–ocean coupled mode featured by quasiperiodic warming and cooling of subsurface and sea surface temperature (SST) over the equatorial Pacific region^{1–4}, which exerts global influences on the weather and climate, marine systems, and land crops^{5–8}. Therefore, previous studies have paid considerable attention to the onset mechanisms essentially crucial for predicting ENSO events. Regarding this issue, some pioneering studies suggested the delayed and recharge oscillator theories, which explain the growth and decay of ENSO from the perspective of self-sustaining oscillatory dynamics^{4,9,10}. From subsequent studies, it was further revealed that the ENSO events could be triggered by high-frequency equatorial wind variabilities, such as westerly wind bursts^{11–13}. Strong equatorial wind events at the sub-seasonal time scale can excite eastward propagating Kelvin wave pulses to promote ENSO development.

In addition to the westerly wind burst, El Niño can be triggered and modulated by the lower-frequency winds, originating from various climate phenomena or modes outside the tropical Pacific, such as the Indian Ocean basin mode^{14,15}, Indian Ocean Dipole^{16–18}, North Tropical Atlantic^{19,20}, and Atlantic warm pool²¹. Interannual variability of these climate modes in remote basins affects seasonal background conditions over the tropical Pacific so that integrated influences of the stochastic wind forcing can lead to lower-frequency oceanic variability.

Besides these tropical variabilities, the North Pacific Oscillation (NPO) is also known as a key contributor to ENSO initiation^{22–29}. The winter mean condition of this extratropical climate mode, which manifests north–south dipolar sea level pressure (SLP) anomalies

over the North Pacific^{30–32}, serves as a good precursor to ENSO developing for the following winter^{26,27,33,34}. To explain this linkage, a previous study³³ first proposed a seasonal footprinting mechanism (SFM) by highlighting the gradual feedback process within the atmospheric boundary layer through interactions between SST and wind anomalies induced by the southern lobe of the NPO, namely the Wind–Evaporation–SST (WES) feedback³⁵. The SFM explains well the persisting growth of wind anomalies once initialized over the subtropical eastern Pacific. However, some features remain unexplained, particularly for the equatorial wind anomalies observed over the western Pacific, nearly concurrent with the SFM-induced subtropical wind anomalies^{13,36} (also see Fig. 2 in our Part I). Thus, studies have pointed out that the SFM-induced SST anomalies, which are constrained over the subtropical eastern North Pacific in winter–spring, do not explain equatorial SST anomalies coupled with equatorial wind anomalies^{36,37}. These arguments suggest that boundary layer processes alone (i.e., WES feedback represented by the SFM) do not fully explain the NPO impacts on the ENSO.

Therefore, in our Part I study, we proposed a mechanism for how the NPO can induce wind anomalies in the tropics. Different from the northward impacts of the NPO on East Asia and North America in the previous studies^{38–40}, we demonstrated that the NPO also induces southward wave activity flux (WAF)⁴¹. Carried by the climatological northerly winds, the wave energy can reach deep tropics and lead to equatorial wind anomalies in the upper troposphere. Thus, the tropical wind anomalies in the lower level concurrent with the SFM-induced subtropical anomalies could be a response to anomalous upper-level winds, promoting convections upon the tropical background conditions that inherently bear the baroclinity^{42–44}. Hence, establishing the NPO-related

¹Collaborative Innovation Center on Forecast and Evaluation of Meteorological Disasters (CIC-FEMD), Nanjing University of Information Science & Technology, Nanjing, China.

²Division of Environmental Science and Engineering, Pohang University of Science & Technology (POSTECH), Pohang, Korea. ³Center for Sustainable Environment Research, Korea Institute of Science and Technology, Seoul, Korea. ⁴Institute for Convergence Research and Education in Advanced Technology, Yonsei University, Seoul, South Korea.

✉email: mksung@kist.re.kr; jskug@postech.ac.kr

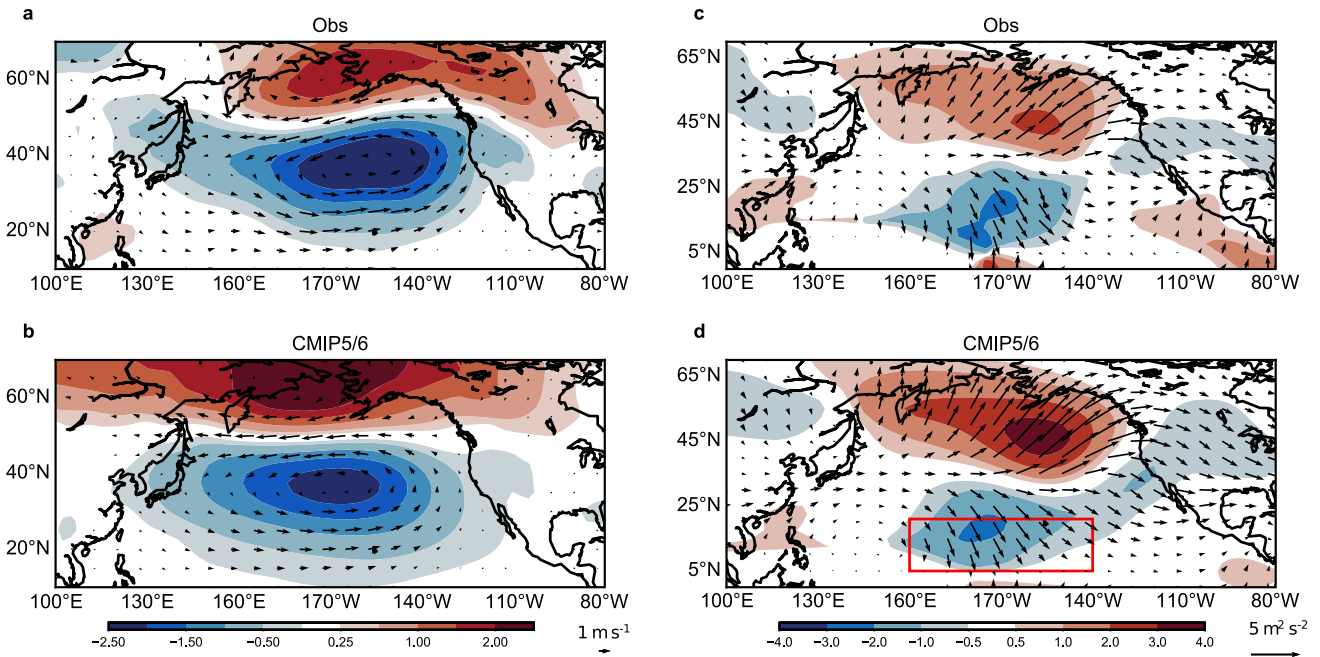


Fig. 1 Composite of DJFJFM1-averaged SLP and 850-hPa winds anomalies and corresponding WAF between positive and negative NPO events. **a** Composite of SLP anomalies (unit: hPa) and 850-hPa wind anomalies (unit: m/s) between positive and negative NPO events for observation. **b** The same as (a) but for the ensemble average of 59 CMIP5/6 models. **c** The observational average of WAF (unit: $5\text{ m}^2\text{ s}^{-2}$) for all selected positive and negative NPO events. **d** The same as (c) but for the ensemble mean of CMIP5/6 models. The shading in (a) and (b) represents the SLP anomalies, whereas it indicates MWF in (c) and (d). The MWF is defined over the region that are marked by a red box in (d).

wind and convection anomalies over tropics favors ENSO event initialization. This process operates independently from the SFM, which manifests through WES³⁵ feedback.

Although we showed clear evidence of the role of the WAF in Part I, we could not draw a concrete conclusion due to the small sample size. The multimodel climate simulations will be a good testbed to verify the observational hypothesis. In addition, the observational findings of the NPO impact on ENSO through the upper-level process may elucidate the large diversity of climate models in reproducing the NPO–ENSO linkage. Previous studies checked the SFM in CMIP5 models and found that only a quarter to one-third of the models shows significant NPO–ENSO linkage determined by SFM intensity^{29,45–47}. The SFM efficiency in inducing ENSO events significantly depends on the climatological locations of the intertropical convergence zone in CMIP5 models⁴⁷. Another recent study showed the SFM in CMIP5 models had large uncertainties in triggering ENSO events that stem from internal climate variability²³. In this regard, it would be meaningful to examine the relative importance of the WAF and the SFM in contributing to the model diversity of simulating the NPO–ENSO linkage.

In this study, using climate models participating in CMIP5/6, we show that the WAF intensity is a crucial factor in determining the NPO–ENSO linkage. Then, the intermodel characteristics will be assessed to corroborate the essential role of the WAF in initiating the ENSO, supporting the conclusion drawn from the observational analysis in Part I. In addition, results in CMIP5 and CMIP6 models will be compared to check the role of WAF in reproducing the NPO–ENSO linkages and to evaluate the relative importance of the WAF and the SFM.

RESULTS

Diversity of the NPO-induced WAF in CMIP5/6 models

Figure 1a shows seasonal December–March (DJFJFM) averaged features of the observed SLP and 850-hPa wind anomalies computed from the composite difference between the positive

and negative NPO phases. It exhibits a typical NPO pattern, regarded as the positive NPO phase in this study, characterized by low-pressure (cyclonic) anomalies to the south and high-pressure (anticyclonic) anomalies over higher latitudes. The results for the multimodel ensemble mean for all CMIP5/6 models show a similar spatial pattern with the observation (Fig. 1b). As shown in our Part I study, the NPO could induce both northward and southward wave energy propagation in the upper level. These features are consistently found in Fig. 1c, d, which, respectively, show the observed and simulated WAF patterns at 300 hPa for the selected NPO cases. The MWF in the model ensemble mean reasonably portrays the observational features in terms of both location and magnitude (shading in Fig. 1c, d) besides diverging WAF patterns from the southern NPO center (vectors). Previous studies have paid attention to the influence of the northern NPO center that leads to extreme climatic events in North America^{40,48}. However, we focus on the southern circulation and equatorward WAF propagation therefrom, as the southward WAF is crucial for the equatorial wind anomalies in both low and upper levels, as identified in Part I.

Figure 2 shows the magnitude of MWF averaged over the 5°N–20°N, 160°E–140°W, a key region reflecting the southward WAF on the tropics (red box in Fig. 1d). Slight changes in domain selection did not affect the robustness of the result. The red bar in Fig. 2 shows the observational MWF, whereas the black bar represents the ensemble mean of MWF for all NPO years. The multimodel-averaged MWF also shows clear equatorward wave propagation, but the magnitude is ~33.6% smaller than the observation. Notably, all models consistently simulate the southward MWF, suggesting that it is quite a robust response to the extratropical NPO-like forcing. However, some models exhibit stronger MWF values than the observation, whereas others have even less than half of the observational intensity, indicating a large diversity in the southward WAF among the CMIP5/6 models (Fig. 2).

Magnitude of southward WAF

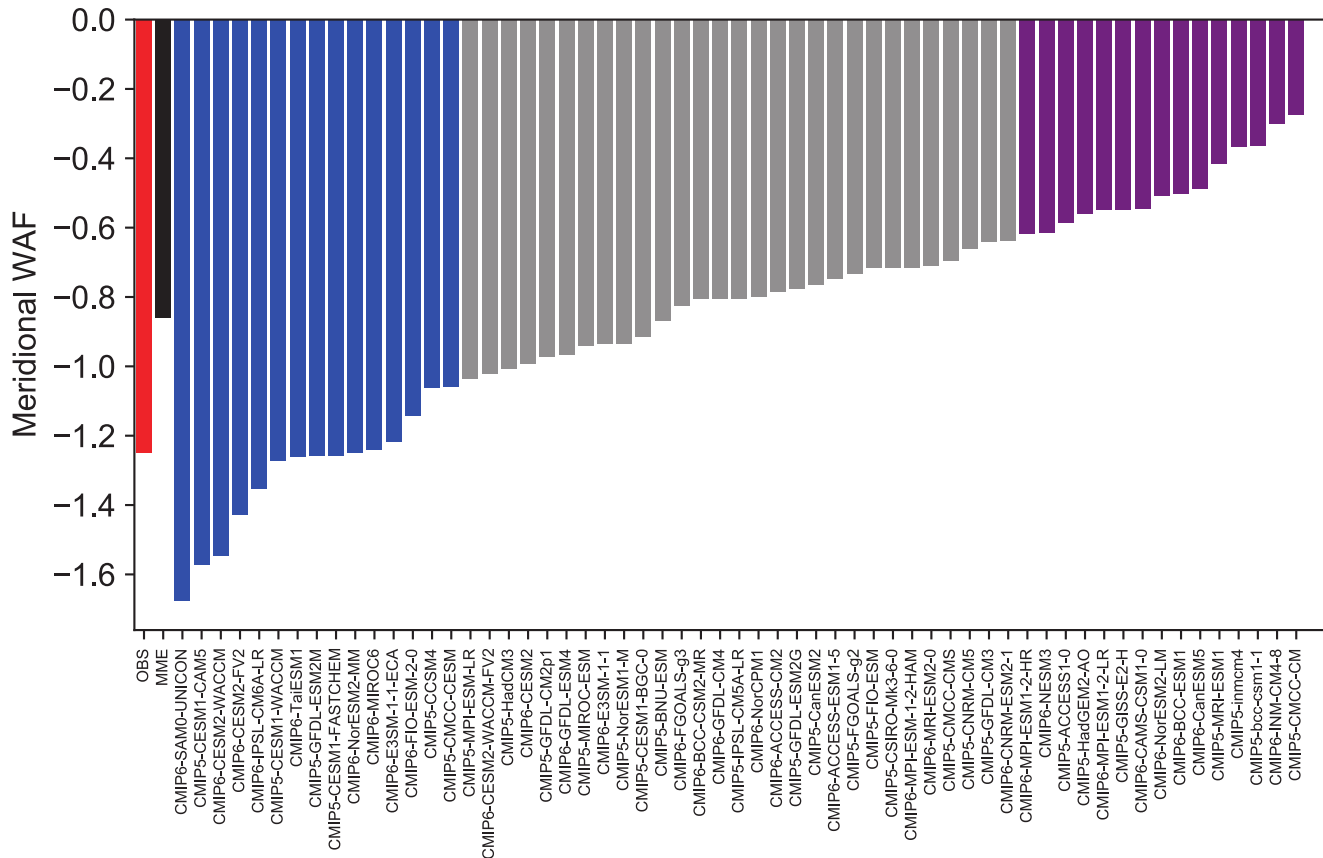


Fig. 2 Magnitude of southward WAF averaged over 160°E–140°W, 5°N–20°N for the observation, 59 CMIP5/6 models, and their ensemble mean. Southward WAF is averaged over 160°E–140°W, 5°N–20°N for all NPO events based on a threshold of 0.5 standard deviations. The red bar represents the observational southward WAF. The blue (purple) bars represent the strong (weak) MWF group, whereas the gray bars represent the rest of the models. Both the strong and weak groups have 15 members of models.

To examine the role of the MWF in the NPO–ENSO linkage, we classified the CMIP5/6 models into two groups: the strong MWF group (blue) and weak MWF group (purple), which include, respectively, 15 models. Figure 3 shows the NPO-related WAF and stream function (SF) anomalies at 300 hPa computed from the ensemble average in the strong and weak groups. The strong MWF group is approximately two times larger in magnitude than that in the weak MWF group (shading in Fig. 3c). Corresponding to the southward WAF, the SF exhibits a distinct anomaly over the tropics; namely, a third tropical anticyclonic cell emerged in addition to the extratropical dipole pattern (Fig. 3d). The weak MWF group also shows the tripole pattern, although the magnitude is relatively weak (Fig. 3e); the tropical anticyclonic cell intensity in the weak MWF group (i.e., the SF anomaly averaged over 0°N–20°N; 130°E–170°W) is only 39.7% compared with that in the strong MWF group, implying a crucial role of the MWF in leading to the tropical anomaly. It seems that the stronger MWF to some extent reflects the stronger intensity of the extratropical dipole, as can be seen from the magnitude difference in SF anomalies over the north Pacific region between the two groups (Fig. 3f). Notably, the large difference in the tropical anticyclonic cell (Fig. 3d) locates in the west of the large difference in the southward WAF (Fig. 3f). This zonal phase difference can be explained by the westward phase propagation of the tropical Rossby waves. The different intensity in the tropical branch leads to distinct equatorial easterly wind anomalies at 300 hPa between the two groups (Fig. 3f, vectors). In the following section, we further show salient differences between the strong

and weak MWF groups that lead to distinct preconditions for the ENSO development.

Distinct MWF impacts on tropical circulations of strong and weak groups

To elucidate the tropical influences of the MWF, we further examined circulation differences between the two model groups, focusing on NPO-related wind (Fig. 4) and precipitation/SST (Fig. 5) anomalies. During the positive NPO phases, in the upper level (300 hPa), an anomalous anticyclonic circulation is established over the tropical Pacific (0°N–20°N), which is more prominent in the strong MWF group (Fig. 4a). Although the weak MWF group shows a similar wind pattern (Fig. 4b), the magnitude was significantly weaker. From the difference map (Fig. 4c), stronger easterly wind anomalies appear over the equatorial western Pacific in the strong MWF group. As for the lower-level winds, the NPO-induced strong cyclonic circulation anomalies over middle latitudes in both the strong and weak MWF groups (Fig. 4d, e). However, a sharp difference between the two groups is found over the equatorial western Pacific that the westerly wind anomalies are extended along the equator only in the strong MWF group (Fig. 4f). The equatorial westerly winds anomalies during winter–spring are crucial for triggering the positive SST anomalies over the tropical Pacific region to initiate ENSO. Although the equatorial easterly anomalies exist in the eastern Pacific, their magnitude was weak and the maximum location is in the Southern Hemisphere. The differences between the two groups are more prominent from the monthly evolution of wind

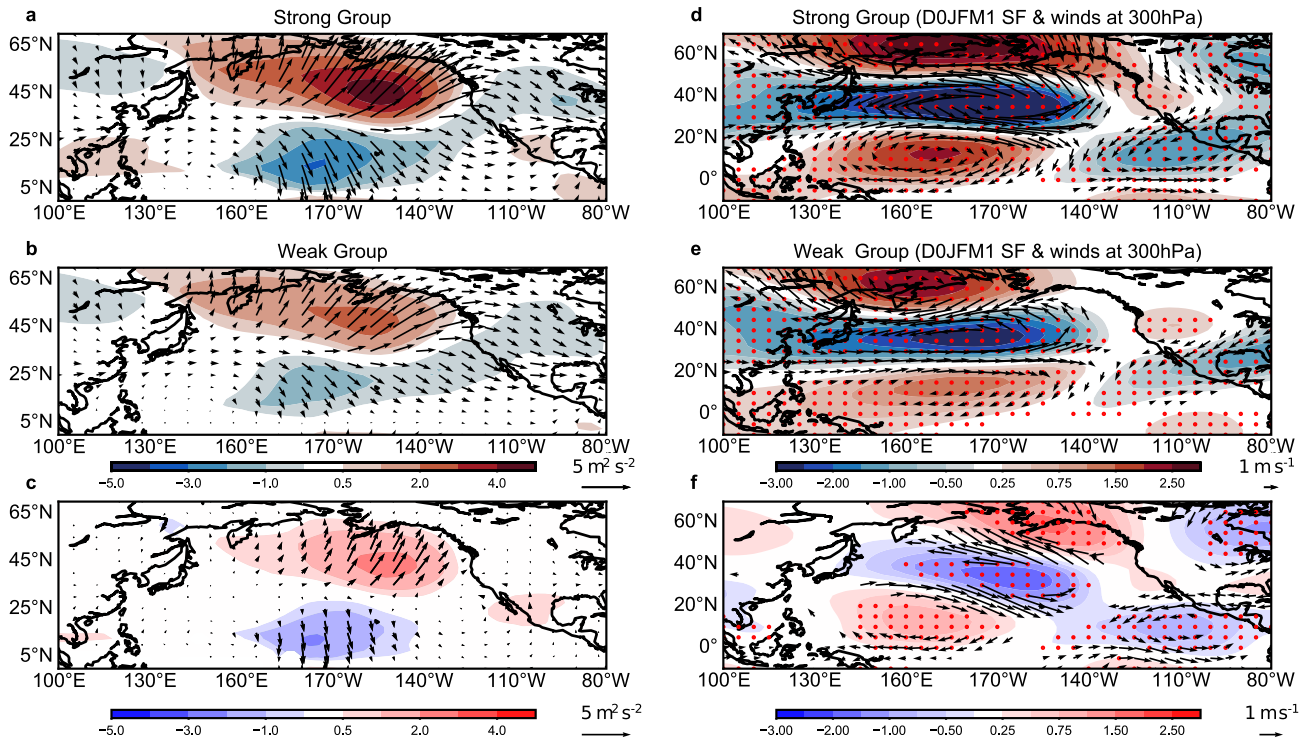


Fig. 3 Composite of DOJFM1 WAF (left) and 300-hPa wind and SF anomalies (right) for the strong and weak MWF groups as well as the differences between groups. **a** The 300-hPa WAF for NPO events in the strong MWF group. **b** The 300-hPa WAF for NPO events in the weak MWF group. **c** The difference between the strong and weak MWF groups. **d, e** Composite difference of DOJFM1 300-hPa wind (unit: m/s) and SF (unit: $10^6 \text{ m}^2 \text{ s}^{-2}$) anomalies between positive and negative NPO events for the strong and weak MWF groups, respectively. **f** The difference of 300-hPa wind and SF anomalies between the two groups. The shading in the left panel represents the MWF, whereas it is the SF in the right panel. The vectors are shown only with the zonal wind above 90% confidence level, and the dots represent the areas of SF above 90% confidence level.

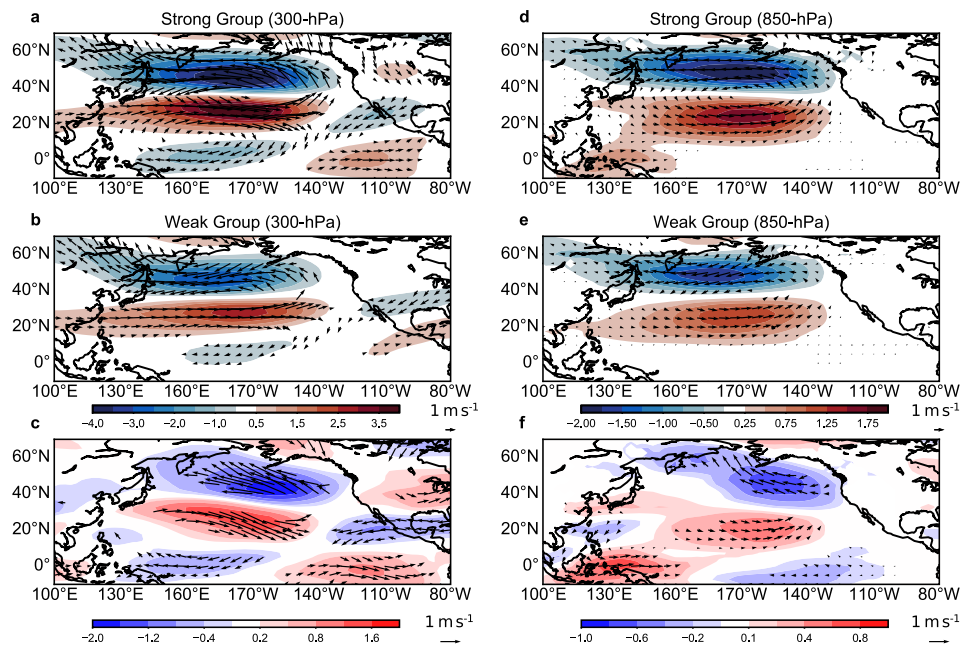


Fig. 4 Composite of zonal wind at 300 hPa (left) and 850 hPa (right) for the strong and weak MWF groups. Composite difference of 300-hPa wind (vectors) and zonal wind anomalies (shading) between positive and negative NPO events for **(a)** strong group and **(b)** weak group. **c** The difference of 300-hPa wind anomalies between the strong and weak MWF groups. **d–f** is the same as **(a–c)** but for 850-hPa wind anomalies. The vectors are shown only with the zonal wind above the 90% confidence level.

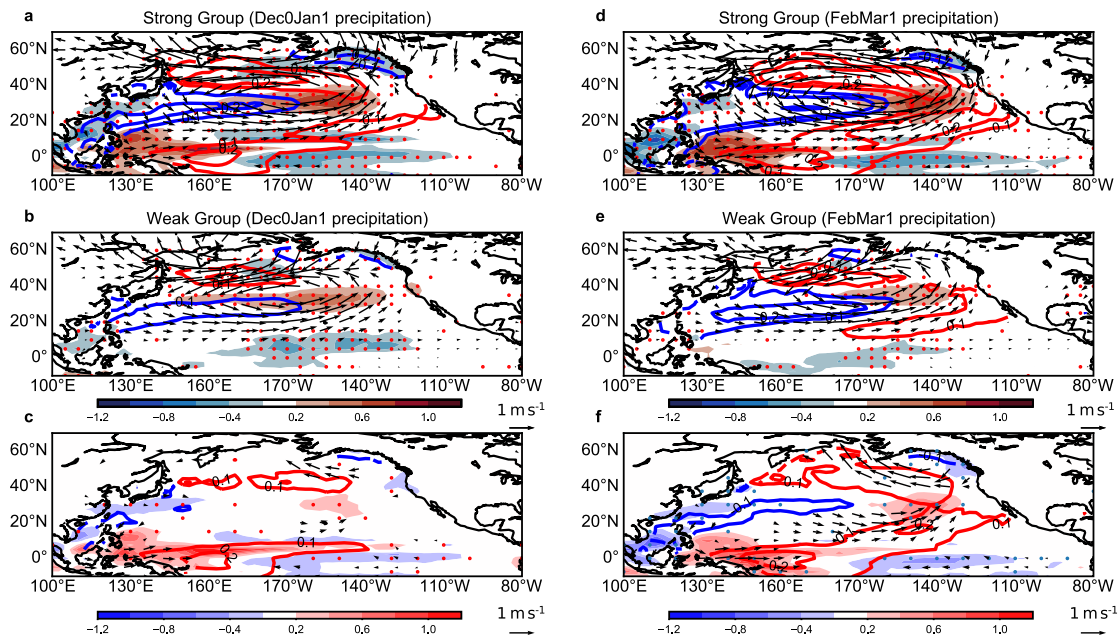


Fig. 5 Composite of SST, 850-hPa wind, and precipitation anomalies during December–January (left) and February–March (right) for the strong and weak MWF groups. **a** Composite difference of SST (contour), 850-hPa wind (vector), and precipitation (shading) anomalies between positive and negative NPO events during December–January for the strong MWF group. **b** Same as (a) but for the weak MWF group. **c** Difference between the strong and weak MWF groups during December–January. **d–f** Same as (a–c) but for February–March. The dots represent areas above the 90% confidence level for the precipitation, and the vectors are shown only with the zonal wind above the 90% confidence level.

anomalies as shown in Supplementary Fig. 1. Clearly, the 850-hPa westerly wind anomalies are strong during DJFM1 season in the Strong group but weak in the Weak group. The low-level westerly wind anomalies sustain and intensify in the following months in the Strong group. At the upper level, the MWF-induced easterly wind anomalies over the western Pacific are significant and strong. Obviously, the low-level and upper-level winds bear the first baroclinic mode over the tropics.

These circulation changes are coupled with the precipitation over the Pacific. During the early winter of positive NPO (December–January; DJJ1), precipitation increases over midlatitudes and decreases over both high and low latitudes common to the strong and weak MWF groups (Fig. 5a, b). However, a significant difference between the two groups is found over the tropical western Pacific; enhanced precipitation is prominent for the strong MWF group (Fig. 5a), but no significant change is found for the weak MWF group (Fig. 5b), indicating that the western Pacific precipitation is enhanced when the southward WAF is strong. This suggests that the extratropical circulation can modulate tropical precipitation through upper-level wave energy propagation. We further investigated the monthly evolution of precipitation anomalies over the tropical WP and subtropical ENP as shown in (Supplementary Fig. 2). In the Strong group, the NPO-induced positive precipitation anomalies is pronounced over both tropical WP and subtropical ENP during DJJFM1. Afterward, the precipitation anomalies decline during the spring and summer seasons and grow back in ND1J2 along with the development of El Niño. The suppressed precipitation during summer is probably because the climatological intertropical convergence zone shifts northward in this season, indicating a limitation of this regional approach. On the contrary, in the Weak group, although the NPO induces considerable precipitation anomalies over the subtropical ENP, the signal does not propagate to the tropical Pacific without the aid of MWF. It is not yet clear how the MWF can dynamically modulate the western tropical Pacific precipitation. Presumably, the seasonal background condition of the Pacific intertropical convergence zone, which locates near the equator in

this season, could allow a favorable condition for the upper-level disturbance to lead to active convection response along the equator, whereas the off-equatorial convective response will be weak under the background sinking motion prevailing over the off-equatorial Pacific. In addition, several studies have pointed out that easterly vertical wind shear in the equatorial region is related to strong high-frequency variability conducive to ENSO development^{44,49–53}. Although the exact mechanism requires further study, the lower-level equatorial westerly wind anomaly, building to vertically baroclinic structure with the upper-level easterly wind, is well-matched with the increased precipitation (Figs. 4d and 5a). Given that the positive precipitation and SST anomalies could induce the Gill-type response⁵⁴, the resultant cyclonic (anticyclonic) circulation response in the lower (upper) level over the western tropical Pacific could intensify the equatorial westerly (easterly) wind. This relation suggests that the precipitation anomalies play a role in enhancing the equatorial wind structures in turn. Therefore, from December–January (Fig. 5c) to February–March (Fig. 5f), the equatorial westerly wind anomalies intensify and extend eastward in the strong MWF group with the enhanced precipitation, favoring the ENSO development in the subsequent season.

Previous studies have shown that the SFM plays a role in triggering the ENSO events. Westerly wind and increased precipitation anomalies over the eastern North Pacific show the SFM-related process in December–January (Fig. 5a). The analogous process also works in the weak MWF group (Fig. 5b), but the difference between the strong and weak MWF groups was not prominent during this season. It is worth noting that the increased precipitation anomalies over the equatorial western Pacific are well coupled with the positive SST anomalies (Fig. 5a) whereas the positive SST anomalies over the subtropical Eastern North Pacific (ENP) are separated from those over the western Pacific (Supplementary Fig. 3), implying that the SFM is still constrained over the subtropical ENP in the strong group. Over time, the difference increases (Fig. 5f), and westerly anomalies become prevalent over the subtropical and central tropical Pacific in late

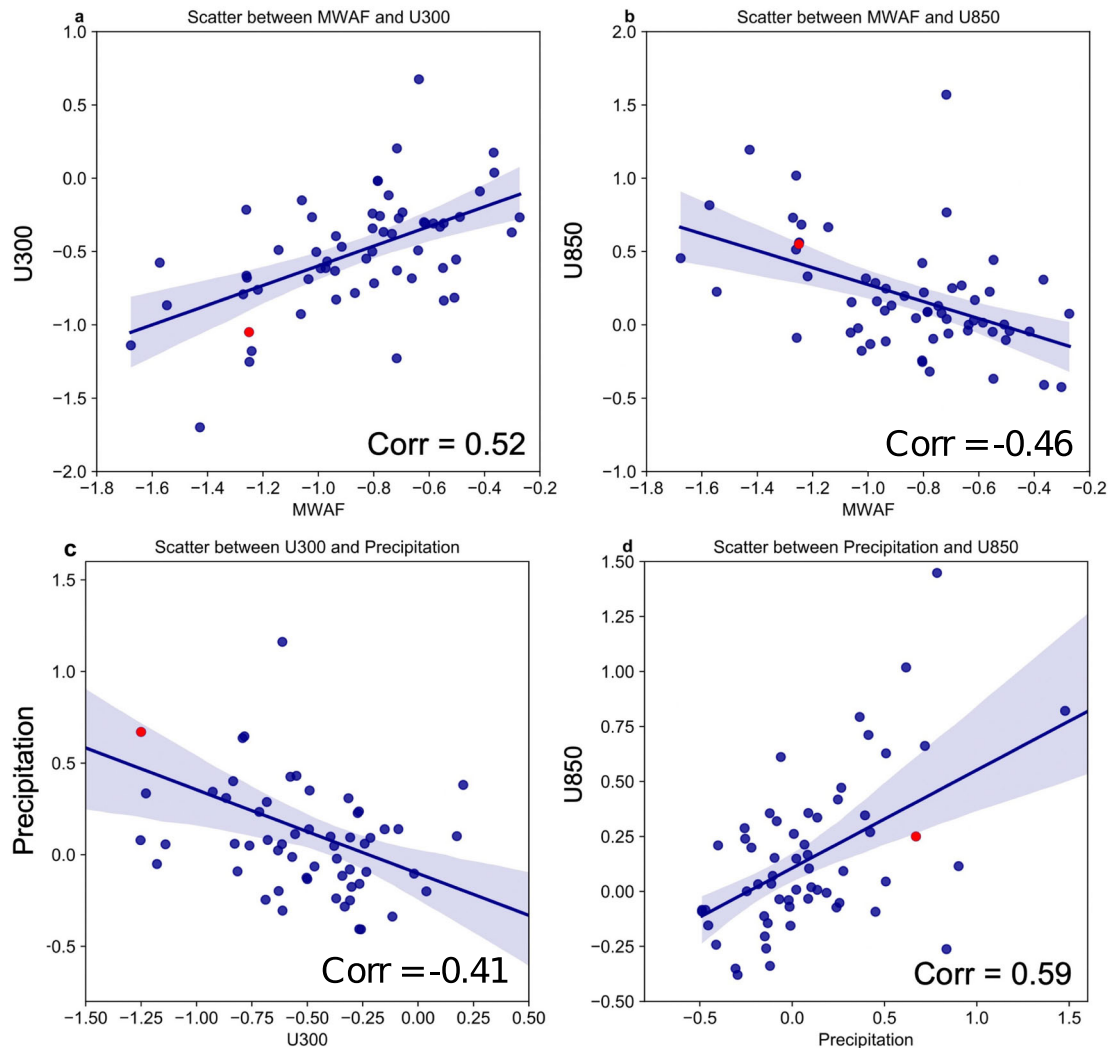


Fig. 6 Intermodel relationship of the MWF versus winds and of precipitation versus winds for selected NPO events. **a** Scatter diagram between MWF for NPO events and corresponding 300-hPa zonal wind anomalies DOJFM1-averaged over 130°E–170°E, 5°S–5°N. **b** The same as (a) but for the 850-hPa westerly wind anomalies averaged over 120°E–160°E, 5°S–5°N, and 300-hPa zonal wind anomalies. **c** Same as (a) but for the precipitation averaged over 120°E–160°E, 5°S–5°N, and 300-hPa zonal wind anomalies. **d** Same as (a) but for the precipitation and 850-hPa wind anomalies. The red dots show the observations while the blue dots represent the CMIP5/6 models. Linear regression lines are shown with their 90% confidence intervals (shaded) using the bootstrap method.

winter (February–March) in the strong MWF group. These differences between the strong and weak MWF groups associated with the SFM might be ascribed to the distinct intensity of the NPO in the two groups to some extent. Nonetheless, no significant tropical anomaly was induced in the weak MWF group, although the SFM works in February–March (Fig. 5e). By contrast, the equatorial westerly wind anomalies were established in December–January (Fig. 5a), which was far earlier than the wind anomalies induced by the “SST footprint” dominating the tropics. The result suggests that the SFM process alone cannot fully explain the equatorial wind anomalies. We will show further the relative importance of MWF and SFM in triggering ENSO in the following section.

So far, we have shown that the upper- and lower-level equatorial wind anomalies are clearly different between the strong and weak MWF groups; now, we check the intermodel relationship between the DOJFM1 MWF intensity and zonal wind averaged over equatorial western Pacific (Fig. 6). A pronounced linear relation is found in Fig. 6a, which indicated that climate models with strong equatorward MWF tend to simulate larger easterly wind anomalies in the upper level over the equatorial

Pacific. The correlation coefficient between the MWF and equatorial easterly wind reached 0.52 for the 59 models, which is significant at the 99% confidence level. In addition, the MWF has a significant correlation with the zonal wind anomalies at 850 hPa ($r = -0.46$; Fig. 6b). Moreover, we checked the intermodel relationship between upper-level easterly wind and precipitation anomalies over the tropical western Pacific (Fig. 6c), which bears a significant correlation ($r = -0.41$). Previous studies^{42,44} verified that the low-frequency upper-level easterly wind anomalies can induce baroclinic structure response through convective low-level convergence feedback. The low-level westerly wind and precipitation are thus largely enhanced (Fig. 6d) in response to the upper-level easterly wind anomalies. These linear relations suggest that the equatorward NPO-related WAF is, in general, a crucial factor in determining equatorial wind anomalies during winter within the climate models in CMIP5/6. The seasonal dependency of the NPO influence is pronounced only in the wintertime because the NPO growth is favored by a strong background potential vorticity gradient near the jet stream⁵⁵.

The varied MWF among climate models and consequent large diversity in the equatorial wind anomalies can lead to different

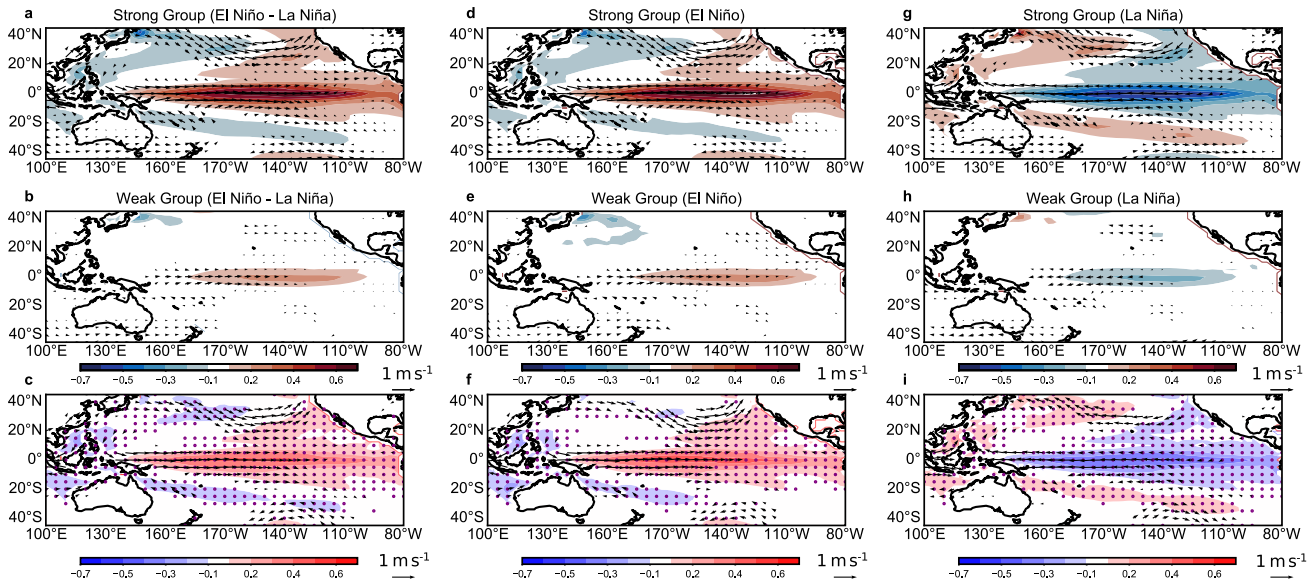


Fig. 7 Composite of subsequent D1JF2-averaged 850-hPa wind and SST anomalies for the strong and weak MWF groups as well as the differences between groups. **a, b** Composite difference of subsequent D1JF2-averaged 850-hPa wind (unit: m s^{-1}) and SST (unit: $^{\circ}\text{C}$) anomalies between the strong and weak MWF groups, respectively. **c** Differences of wind and SST anomalies between the strong (a) and weak (b) MWF groups. **d, e** Composite of 850-hPa wind and SST anomalies during positive NPO phases for the strong (d) and weak (e) MWF groups. **f** Differences of wind and SST anomalies between the strong (d) and weak (e) MWF groups. **g–i** Same as (d–f) but for negative NPO phases. The dots represent areas above the 90% confidence level for the SST, and the vectors are shown only with the zonal wind above the 90% confidence level.

oceanic responses in the following winter. To show this, we first compared the SST anomalies in December–February (D1JF2) of the following winter for the strong and weak MWF groups, respectively (Fig. 7). For consistency with the previous analyses, in Fig. 7a–c, we present the results computed from the difference between positive and negative NPO phases. In the strong MWF group (Fig. 7a), the SST and wind anomalies show pronounced warming and prevalent westerly wind anomalies over the central and eastern equatorial Pacific, which are typical characteristics of the ENSO. In the weak MWF group (Fig. 7b), similar patterns of the anomalies also appear, but their amplitudes are much weaker. Comparing the strong and weak MWF groups (Fig. 7c), the significant differences in the SST (dotted area) support that the influence of the extratropical variability conveyed through the MWF, can trigger a significant ENSO development. Although the NPO-related energy propagation is available only for winter and early spring, once the westerly wind and SST anomalies are initiated, they can intensify afterward due to the positive feedback inherent in the tropical climate system, such as Bjerknes feedback¹. Direct modulation through the wave energy propagation operates symmetrically for the positive and negative NPO phases. When we compare the strong and weak MWF groups for the positive NPO phase alone (Fig. 7d–f), the result shows a robust ENSO pattern for the stronger MWF group. Likewise, for the negative NPO phase (Fig. 7g–i), ENSO development is prominent only in the strong MWF group.

The above pronounced oceanic responses altered by the MWF are a widely observed characteristic in the CMIP5/6 models. Figure 8 shows scatter plots for Niño3.4 SST against the equatorward WAF for all CMIP5/6 models. Apparently, it exhibits a significant linear intermodel relationship ($r = -0.57$), when estimated from the difference between positive and negative NPO phases (Fig. 8a). The result suggests that the stronger the MWF is, the larger the ENSO amplitude will be in the climate models. Results for the positive and negative NPO phases alone also show prominent linear relations, supporting symmetrical effects of MWF in leading to El Niño and La Niña (Fig. 8b, c). This general relation among the CMIP5/6 models corroborates that the NPO impacts on

subsequent winter ENSO events significantly depend on the magnitude of MWF. Although the stronger energy flux tends to be accompanied by stronger NPO, the NPO intensity itself was not a critical factor in determining the NPO–ENSO linkage. When we checked the relationship between NPO intensity and subsequent winter ENSO index, their correlation coefficient was weak and even negative ($r = -0.22$). This suggests that the magnitude of the MWF is regulated by complex processes apart from the NPO intensity. In the next section, the role of background flow conditions in the CMIP5/6 models is examined regarding the equatorward energy propagation.

Possible reasons for the different WAF behavior in CMIP5/6 models

In our Part I study, based on the observational analysis, we delineated how background flow over the North Pacific could propagate the wave energy of the NPO toward the equator. The large diversity of the equatorward WAF across the CMIP5/6 models might also be associated with the background flow condition. The formula of WAF suggests that wave energy propagation is largely carried by climatological winds. So, we further checked the climatological winds, focusing on the MWF, and the difference between the strong and weak MWF groups (Fig. 9a, b). The horizontal distribution of the climatological meridional winds at 300 hPa showed prevailing southerly winds (red shading) over the northern flank of the jet stream and northerly winds (blue shading) over the opposite flank, guiding the wave energy propagation northward or southward. This background flow structure is common to both groups, but in the strong MWF group, the climatological northerly wind tends to be stronger over the subtropical region (180°W – 140°W , 0°N – 20°N) than that in the weak MWF group (Fig. 9c). It is inferred that a stronger background northerly wind would contribute to a stronger equatorward WAF. A scatter diagram in Fig. 10a supports the significant role of the mean meridional wind; the overall linear relation suggests that climatological northerly winds over the tropical key region could affect the MWF intensity, thus possibly

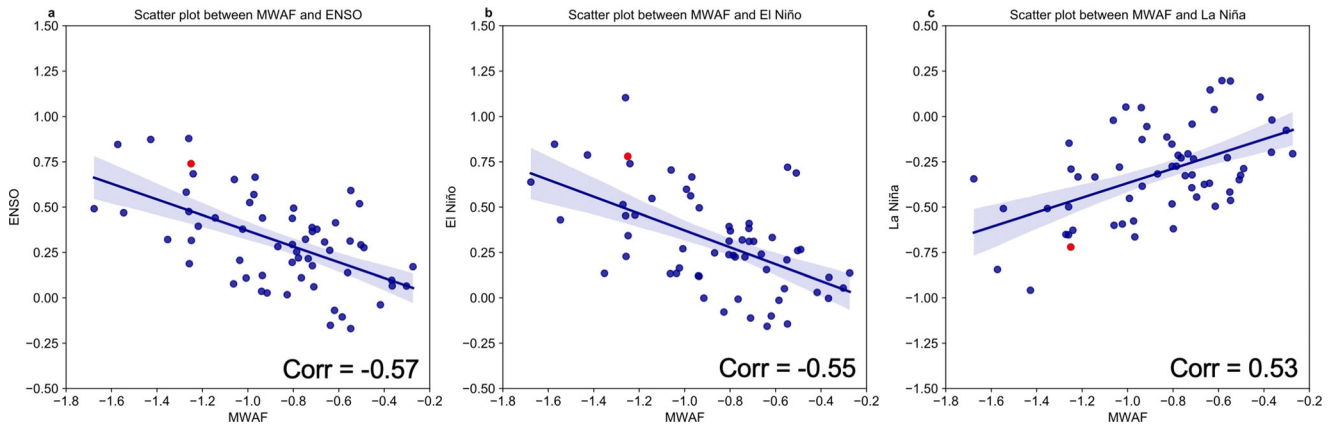


Fig. 8 Intermodel relationship between Niño3.4 index and MWF for selected NPO events. **a** Scatter plot between DJFM1 MWF for NPO events and DJF2 SST anomalies over Niño3.4 (5°S–5°N, 120°W–170°W) region presented for the difference between positive and negative NPO phases. **b** Same as **(a)** but only for all positive NPO phases. **c** The same as **(b)** but for all negative NPO phases. The red dots show the observations while the blue dots represent the CMIP5/6 models. Linear regression lines are shown with their 90% confidence intervals (shaded) using the bootstrap method.

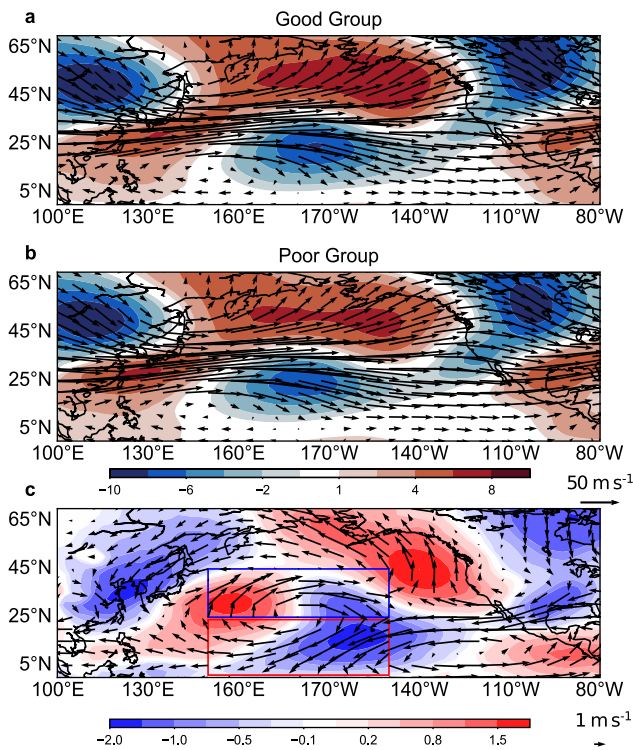


Fig. 9 Climatological winds in the strong and weak MWF groups and their differences. **a, b** Climatological winds (vector) at 300-hPa in the strong and weak MWF groups, respectively. **c** The differences between the strong and weak MWF groups. The shading in **(a)** and **(b)** represent the climatological meridional winds, whereas it indicates the difference in the meridional wind between the strong and weak MWF groups in **(c)**. The meridional shear of zonal wind is calculated from the difference of climatological zonal wind over 25°N–45°N, 150°E–150°W (blue box) and EQ–25°N, 150°E–150°W (red box). The green dots in **(c)** represent areas significantly above the 90% confidence level when comparing two groups with each containing 15 members.

contributing to the large diversity in the tropical impact of the NPO across the CMIP5/6 models. A correlation coefficient for this intermodel relationship reached 0.48, which was significant at a 99% confidence level. This result, obtained from the intermodel

comparison, agrees with the observational analysis of $F_{y2} (= V[u'^2 + \psi' \frac{\partial u'}{\partial \phi}])$ that the climatological meridional winds convey the influence of the NPO to the tropics.

Besides the background northerly wind, MWF depends on the horizontal shape of the eddy; given $F_{y1} (= U[-u'v' - \cos \phi \psi' \frac{\partial v'}{\partial \phi}])$, under westerly background flow condition ($U > 0$), wave energy propagated southward when an eddy was deformed to realize a southwest–northeast horizontal tilt (i.e., $u'v' > 0$ and $\psi' \frac{\partial v'}{\partial \phi} > 0$). In Fig. 9c, the strong MWF group models showed a strong anticyclonic shear over the southern flank of the jet stream. Accordingly, the background wind in the strong MWF models tends to have stronger meridional shear of mean zonal wind within the subtropical Pacific, i.e., stronger easterly wind in the tropics and westerly wind in the subtropics. This background wind shear can increase equatorward wave energy propagation by driving the southwest–northeast tilt of circulation branches of the NPO. This zonal wind shear contribution in the CMIP5/6 models can be found in Fig. 10b. The overall linear distribution of 59 model values supports that the MWF in the climate models is significantly correlated with the zonal wind shear as well ($r = -0.38$). This result verified that the large diversity of the MWF in the CMIP5/6 models could to some extent stem from varied background wind characteristics in individual climate models.

Relative importance of MWF and SFM in CMIP5/6 models

Previous studies have shown the role of the SFM in triggering the following winter ENSO events. Now we examine the intermodel relationship between SFM and ENSO, and compare it with the result for the MWF. The SFM intensity is defined as the difference of SST anomalies between subtropical ENP (120°W–150°W, 10°N–25°N) and equatorial Eastern Pacific (90°W–120°W, 5°S–5°N). Here, we note that the ENSO signal (represented by Niño3.4 index) was removed based on previous work⁵⁶. After the ENSO signal was removed, the SFM intensity (Supplementary Fig. 4) could be largely represented by the SST anomalies over the subtropical ENP and equatorial Eastern Pacific, which is also referred to as the Pacific Meridional Mode (PMM)^{36,56,57}. We also checked the SFM intensity only using SST anomalies over the subtropical ENP and the result is consistent. Same as the MWF, we classified the weak (blue) and strong (purple) groups based on the magnitude of the SFM and compared the following ENSO signal in the two groups (Supplementary Fig. 4). The SFM index reasonably captures the influence on ENSO. However, the ENSO magnitude is weaker in the strong group compared with the

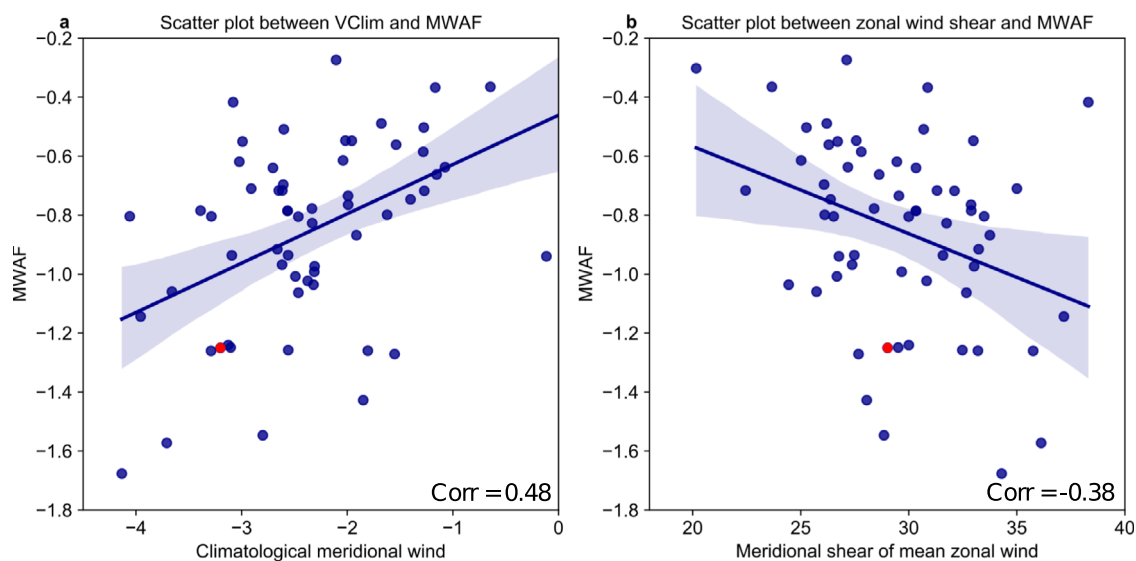


Fig. 10 Relation of climatological wind and MWF in CMIP5/6. **a** Scatter plot of climatological meridional winds over 180°W – 140°W , EQ – 20°N versus MWF averaged over 160°E – 140°W , 5°N – 20°N for 59 models. **b** Scatter plot of meridional shear of zonal wind versus MWF. Meridional shear of zonal wind is calculated from the difference of climatological zonal wind in Fig. 9c. Linear regression lines are shown with their 90% confidence intervals (shaded) using the bootstrap method.

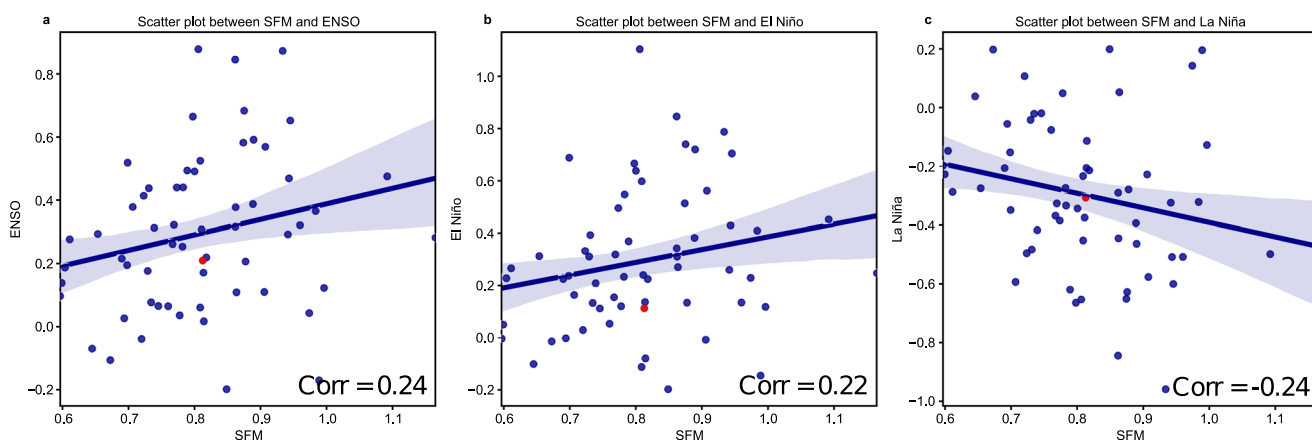


Fig. 11 Intermodel relationship between Niño3.4 index and SFM index for selected NPO events. **a** Scatter plot of the SST anomalies over Niño3.4 region and the SFM computed for the differences between positive and negative NPO phases. **b** Same as (a) but only for all positive NPO phases. **c** Same as (b) but for all negative NPO phases. Linear regression lines are shown with their 90% confidence intervals (shaded) tested by the bootstrap method. The correlation coefficients are 0.24, 0.22, and -0.23 , respectively for (a), (b), and (c).

MWAF group (Supplementary Fig. 5). Moreover, the ENSO in the strong group is not well separated from the weak group since the difference of SST anomalies is weak (Supplementary Fig. 5). So, we further checked the intermodel relationship between SFM intensity and ENSO magnitude (Fig. 11). The result shows overall weak correlation ($r = 0.24$), which is not significant at the 95% confidence level, indicating that the diverse NPO–ENSO relation in CMIP5/6 is not significantly modulated by the SFM. We note that the results did not largely alter according to the SFM index definition; when we utilized the SST anomalies only of the subtropical ENP or those of February–March, the results were overall consistent (data not shown).

We finally compare the contribution of the MWAF and SFM processes to yielding NPO–ENSO relationship from the intermodel spread. Since we are using a relatively large model sample (59 models), we can statistically separate how much each process contributes to the intermodel diversity of the NPO–ENSO relation, which implies the relative importance of the MWAF and SFM.

Figure 12a shows the scatter plot of the MWAF and SFM with the NPO–ENSO relationship marked with different colors and sizes. The significant correlation marked between the MWAF and the SFM ($r = -0.33$) shows that the two major processes linking the NPO and ENSO are not completely independent, presumably because both are affected by the NPO intensity. However, as we showed in Fig. 8, the intermodel relation of the MWAF and ENSO exhibits a higher correlation ($\text{corr} = -0.57$) than that of the SFM ($\text{corr} = 0.24$), which underpins the crucial role of the MWAF in delivering NPO influence to the tropics. When we further removed the SFM signal from the MWAF, the MWAF still present significant linear intermodel relation with the correlation between DJFM1 NPO and following winter ENSO (Fig. 12b). The result substantiates that the stronger MWAF models have, the NPO better triggers subsequent ENSO, irrespective of the SFM intensity. By contrast, when we further removed the MWAF signal from the SFM, we could no longer find that the SFM contribute to the NPO–ENSO connections ($r = -0.01$; Fig. 12c). This demonstrates that the

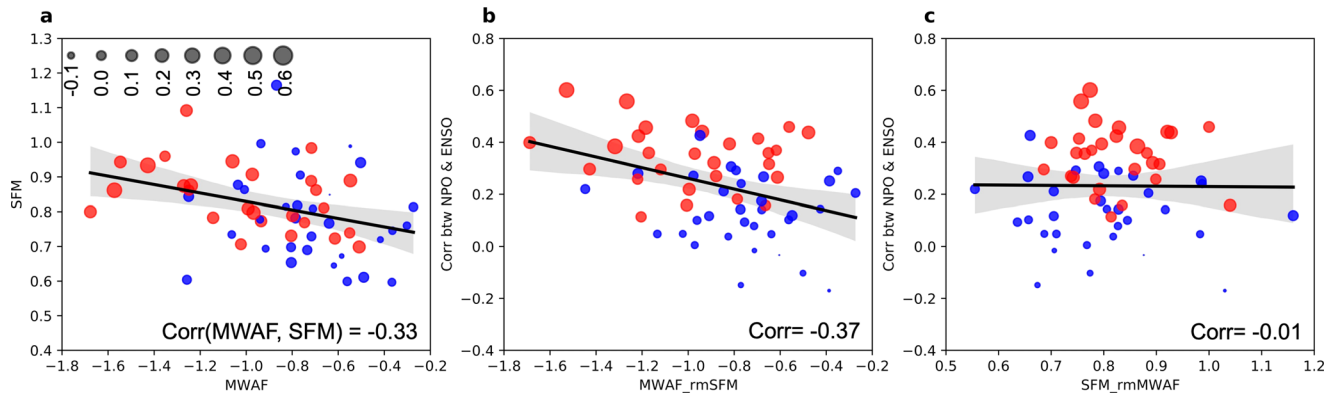


Fig. 12 Scatter diagrams showing the relative importance of MWF and SFM. **a** The scatter plot of MWF and SFM with and correlation coefficients between DJFM1-averaged NPO and following winter ENSO for each model marked as different sizes of dots. **b** The scatter plot of MWF without SFM signal (linearly removed) and correlation coefficients between NPO and ENSO. **c** The scatter plot of SFM without the MWF signal (linearly removed) and correlation coefficients between NPO and ENSO. Here, the correlations between the two-dimensional variables are shown in each subplot and the red (blue) dots represent the ENSO magnitude above (below) the average of 59 models.

MWF plays a significant and independent role in inducing ENSO events while the SFM may play a minor role in leading to the diverse NPO–ENSO intermodel relationships.

DISCUSSION

Previous studies have found that the NPO in winter can exert a pronounced impact on subsequent winter ENSO events. This modulation effect from the extratropical Pacific has been explained by feedback processes within the atmospheric boundary layer and oceanic mixed layer referred to as the SFM^{28,29}. In the companion work (i.e., Part I), we proposed a new mechanism to convey the influence of the NPO to the tropics via upper-level wave energy propagation. Based on the observational data, we found the equatorward WAF can induce both upper- and lower-level wind anomalies in the equatorial Pacific during winter, initiating ENSO events.

In this study, we substantiated the impact of WAF during NPO years on ENSO events by comparing CMIP5/6 climate models in simulating the MWF and consequent responses over the tropical Pacific. We found a significant diversity across climate models in terms of the MWF during NPO winters and that such differences are responsible for distinct ENSO responses during the subsequent winter ($r = -0.57$). This significant relation results from the equatorial wind anomalies responding to the southward propagation of WAF. By separating the CMIP5/6 models into two groups based on the MWF intensity, the strong and weak MWF groups, we found that stronger tropical wind and precipitation anomalies are induced in the strong MWF group models than in the weak MWF group. The differences in the equatorial wind and precipitation were pronounced, even in the early winter, before the influence of the SFM conveyed from the subtropics to the equatorial Pacific. This prompt response in the tropics induced by the MWF during early winter is notable because it could resolve the issue that is unexplained in existing studies regarding the early development of equatorial anomalies observed during NPO winters^{36,37,39}. These results support that the tropical responses during NPO winters can be attributed to the role of the equatorward WAF.

By analyzing climatological wind in the CMIP5/6 models, we further found that the diverse MWF intensities across the models to some extent stem from the distinct background flow conditions over the North Pacific. The climatological northerly wind located over the southern flank of the Pacific jet stream acts to carry wave energy of the NPO equatorward. Thus, climate models with stronger climatological northerly wind tended to deliver more energy to the equator, leading to greater atmospheric and oceanic

responses. We further assessed the role of the meridional shear of mean zonal wind that acts to deform circulation branches of the NPO to get a northeast–southwest tilt favoring southward energy propagation. This horizontal deformation effect varying among models contributes to the diversity in the equatorward energy propagation and the tropical response to the NPO.

Lastly, we evaluated the relative importance of the MWF and the SFM in determining the intermodel diversity of the NPO–ENSO relationship in CMIP5/6 models and found a dominant role of the MWF. Though we substantiated the crucial role of the MWF in triggering ENSO events using intermodel diversity of CMIP5/6 models, one may wonder if the equatorial processes triggered by the wave energy flux alone are sufficient to drive ENSO events in the subsequent winter. For a more quantitative evaluation of the contributions from the SFM and WAF, further research *via* numerical experiments is required, and we leave this for future work. It is noted that the previous winter ENSO signal has been removed from both NPO index and circulation fields since the ENSO could also affect the NPO^{58–60}.

In this study, when classifying the strong and weak MWF groups, both CMIP5 and CMIP6 models were used. The relative numbers of the CMIP5 and CMIP6 models incorporated in the strong and weak MWF groups may provide an indirect measure to assess an improvement between the two intercomparison projects in simulating the extratropical influence toward the tropics. The result finds that, among 59 CMIP5/6 models, 7 (8) CMIP6 models were classified into the 15 strong (weak) groups, ostensibly indicating that there was no significant difference or improvement between CMIP5 and CMIP6 models in terms of the MWF. These comparable results between the CMIP5 and CMIP6 models suggested that climatological mean flow characteristics over the North Pacific, crucial for carrying the wave energy equatorward, did not show significant advances between the climate model generations. However, behind the diverse results of the climate models, the influences of both mean bias and long-term internal variabilities were involved. Therefore, for stricter evaluations of the CMIP5 and CMIP6 performances regarding the extratropical–tropical linkage, studies on the role of long-term internal variability are required. In addition, decadal variations of the NPO–ENSO linkages, identified from observational analyses^{26,47}, deserve attention from the perspective of long-term changes in the North Pacific background flow. The roles of internal climate variabilities leading to changes in the atmospheric background conditions need to be accessed to further elucidate the seasonal prediction and future projection of ENSO.

Table 1. CMIP5 and CMIP6 models used in this study.

OBS&CMIP5 model	Case number (0.5/0.7 SD)	CMIP6 model	Case number (0.5/0.7 SD)
OBS	39/31	ACCESS-CM2	44/32
CMCC-CM	40/32	ACCESS-ESM1-5	42/31
CESM1-CAM5	40/31	BCC-CSM2-MR	35/27
CanESM2	41/30	BCC-ESM1	42/34
GFDL-ESM2M	39/34	CAMS-CSM1-0	39/32
HadCM3	33/26	CanESM5	44/34
GFDL-ESM2G	40/30	CESM2-FV2	34/25
CNRM-CM5	41/35	CESM2-WACCM-FV2	47/40
FGOALS-g2	43/30	CESM2-WACCM	43/32
CMCC-CESM	37/33	CESM2	45/39
ACCESS1-0	40/36	CNRM-ESM2-1	38/32
CESM1-WACCM	39/34	E3SM-1-1	37/28
IPSL-CM5A-LR	43/34	E3SM-1-1-ECA	39/32
CMCC-CMS	41/32	FGOALS-g3	39/35
NorESM1-M	42/34	FIO-ESM-2-0	38/32
GFDL-CM2p1	49/36	GFDL-CM4	45/33
MIROC-ESM	40/35	GFDL-ESM4	39/29
CESM1-FASTCHEM	39/27	INM-CM4-8	37/31
GFDL-CM3	35/28	IPSL-CM6A-LR	39/30
CCSM4	37/28	MIROC6	37/31
HadGEM2-AO	38/34	MPI-ESM-1-2-HAM	40/32
BCC-CSM1-1	39/32	MPI-ESM1-2-HR	42/30
CESM1-BGC-0	43/33	MPI-ESM1-2-LR	44/36
CSIRO-Mk3-6-0	41/31	MRI-ESM2-0	43/33
BNU-ESM	40/32	NESM3	40/31
MPI-ESM-LR	45/37	NorCPM1	44/36
GISS-E2-H	36/33	NorESM2-LM	39/28
INM-CM4	41/35	NorESM2-MM	38/26
FIO-ESM	41/34	SAM0-UNICON	41/32
MRI-ESM1	40/27	TaiESM1	42/27

The number of cases selected based on respective ± 0.5 and ± 0.7 standard deviation (SD) are shown in the table. Bold values indicate the number of selected cases based on a threshold.

METHODS

Observational and modeling datasets

We analyzed historical simulations from 29 and 30 climate models in the CMIP Phases 5 and 6 (CMIP5/6), respectively (Table 1). The monthly data in CMIP6 cover from 1950 to 2014, whereas those in CMIP5 cover from 1941 to 2005. The data periods were chosen to keep the same time length of 65 years. Since the spatial resolutions were diverse in the CMIP5/6 models, all atmospheric and oceanic datasets were remapped into a $2.5^\circ \times 2.5^\circ$ resolution, and the linear trends were removed before computing the anomalies. As observational references, National Centers for Environmental Prediction/National Centers for Atmospheric Research reanalysis version 1 (NCEP/NCAR v1)⁶¹ was analyzed, whose monthly data span from 1950 to 2014 with a $2.5^\circ \times 2.5^\circ$ horizontal resolution. As an oceanic variable, SST was obtained from the Extended Reconstruction Sea Surface Temperature version 5 (ERSSTv5) data with a $2^\circ \times 2^\circ$ horizontal resolution, which was downloaded from the National Oceanic and Atmospheric Administration (NOAA)⁶².

Statistical and diagnosing methods

It is known that CMIP5/6 models overall well portray the NPO and ENSO basic characteristics such as the dipolar spatial structure of the NPO^{63,64} and winter seasonal locking and spatial pattern of ENSO⁶⁵. Therefore, in our analysis, we follow conventional definitions of the NPO and ENSO adopted in earlier studies. The NPO is defined as the second empirical orthogonal function (EOF) of the DJFM1-averaged SLP anomalies over 20°N – 70°N ; 110°E – 120°W domain, and corresponding principal component timeseries were regarded as the NPO indices. A slight change in seasonal selection or domain for EOF analysis does not significantly alter the results. In two models (CNRM-ESM2-1 and E3SM-1-1-ECA), the characteristic north–south dipole pattern of the NPO was captured in the first or third EOFs, and we considered those as the NPO. We noticed that the ENSO and NPO show a significant simultaneous correlation in some models, indicating the NPO cooccurs with ENSO events. To minimize ENSO's autocorrelation effect from the 1-year lagged ENSO–NPO relation year, the December–February (DJF1) ENSO signal is linearly excluded from the NPO index based on the regression against Niño3.4 (5°S – 5°N ; 120°W – 170°W) SST index^{26,47}. Both the NPO and ENSO indices were normalized when calculating regressed maps or selecting NPO cases. Positive or negative NPO winters were selected when the NPO index exceeded a ± 0.5 standard deviation, thus the number of NPO cases varied among the CMIP5/6 models (Table 1). Although we adopted a relatively low threshold to include enough samples, higher thresholds, such as ± 0.7 standard deviation, provided consistent results (not shown). The SFM intensity is defined as the difference of SST anomalies between subtropical ENP (120°W – 150°W , 10°N – 25°N) and equatorial Eastern Pacific (90°W – 120°W , 5°S – 5°N) after the simultaneous ENSO signal (represented by the Niño3.4 index) is removed, which can reasonably capture the SFM SST anomalies.

Based on DJFM1-averaged stream function (SF) anomalies and climatological winds, the NPO-related horizontal Rossby wave energy propagation could be traced by adopting the WAF⁴¹. The WAF in spherical coordinates can be expressed as follows:

$$\mathbf{WAF} = \frac{p \cos \phi}{2|\mathbf{U}|} \begin{pmatrix} \frac{U}{a^2 \cos^2 \phi} \left[\left(\frac{\partial \psi'}{\partial \lambda} \right)^2 - \psi' \frac{\partial^2 \psi'}{\partial \lambda^2} \right] + \frac{V}{a^2 \cos \phi} \left[\frac{\partial \psi'}{\partial \lambda} \frac{\partial \psi'}{\partial \phi} - \psi' \frac{\partial^2 \psi'}{\partial \lambda \partial \phi} \right] \\ \frac{U}{a^2 \cos \phi} \left[\frac{\partial \psi'}{\partial \lambda} \frac{\partial \psi'}{\partial \phi} - \psi' \frac{\partial^2 \psi'}{\partial \lambda \partial \phi} \right] + \frac{V}{a^2} \left[\left(\frac{\partial \psi'}{\partial \phi} \right)^2 - \psi' \frac{\partial^2 \psi'}{\partial \phi^2} \right] \end{pmatrix} \quad (1)$$

where $\mathbf{U} = (U, V)$ are the climatological zonal and meridional winds, respectively; ψ' is the seasonal SF anomaly associated with the NPO; a , ϕ , and λ are the Earth's radius, latitude, and longitude; p is the air pressure at 1000 hPa. Instead of using a quasi-geostrophic approximation to derive the SF based on geopotential height, we derive the SF anomaly based on the zonal and meridional winds by solving the differential equations $u' = \frac{1}{a} \frac{\partial \psi'}{\partial \phi}$ and $v' = -\frac{1}{a \cos \phi} \frac{\partial \psi'}{\partial \lambda}$. As this study examines the tropical influence of the NPO via energy propagation, we focus on the meridional WAF (MWAF), which can be decomposed as follows:

$$\mathbf{F}_{y1} = \frac{U}{a^2 \cos^2 \phi} \left[\frac{\partial \psi'}{\partial \lambda} \frac{\partial \psi'}{\partial \phi} - \psi' \frac{\partial^2 \psi'}{\partial \lambda \partial \phi} \right] = U \left[-u'v' - \cos \phi \psi' \frac{\partial v'}{\partial \phi} \right] \quad (2)$$

$$\mathbf{F}_{y2} = \frac{V}{a^2} \left[\left(\frac{\partial \psi'}{\partial \phi} \right)^2 - \psi' \frac{\partial^2 \psi'}{\partial \phi^2} \right] = V \left[u'^2 + \psi' \frac{\partial u'}{\partial \phi} \right] \quad (3)$$

where \mathbf{F}_{y1} represents the first part related to the climatological zonal wind (U), and \mathbf{F}_{y2} stands for the second part carried by the climatological meridional wind (V). The formula indicates the meridional energy transport depends on background wind characteristics and horizontal deformation of an eddy. When

displaying the WAF in figures, we presented the values averaged for positive and negative NPO phases, since the NPO-induced WAF has the same sign regardless of the NPO phase; i.e., southward over the tropical region for both positive and negative NPO phases. Besides the WAF, other variables were displayed with the composite differences between positive and negative NPO phases, given the nearly symmetrical composite results.

Statistical significance

In this study, we adopted the two-tailed Student's *t* test with a significance level of 0.1 in all analyses. The bootstrap method with a significance level of 0.1 was used in Figs. 6, 8, 10, 11 and 12. The degree of freedom for the composite between the Strong and Weak models is 28 and 57 for the regression.

DATA AVAILABILITY

The monthly and daily NCEP/NCAR reanalysis data can be downloaded from <https://psl.noaa.gov/data/gridded/data.ncep.reanalysis.html>. The ERSSTv5 dataset is retrieved from NOAA <https://psl.noaa.gov/data/gridded/data.noaa.ersst.v5.html>. The CMIP5/6 datasets are downloaded from <https://data.ceda.ac.uk>.

CODE AVAILABILITY

The source codes for the analysis of this study can be requested from the first author.

Received: 12 June 2022; Accepted: 8 February 2023;

Published online: 27 February 2023

REFERENCES

- Bjerknes, J. Atmospheric teleconnections from the equatorial Pacific. *Mon. Weather Rev.* **97**, 163–172 (1969).
- Philander, S. G. H. El Niño and La Niña. *J. Atmos. Sci.* **42**, 2652–2662 (1985).
- Zebiak, S. E. & Cane, M. A. A model El Niño–Southern oscillation. *Mon. Weather Rev.* **115**, 2262–2278 (1987).
- Jin, F.-F. An equatorial ocean recharge paradigm for ENSO. Part I: conceptual model. *J. Atmos. Sci.* **54**, 811–829 (1997).
- Chen, S. & Yu, B. Projection of winter NPO–following winter ENSO connection in a warming climate: uncertainty due to internal climate variability. *Clim. Change* **162**, 723–740 (2020).
- Anderson, W. B., Seager, R., Baethgen, W., Cane, M. & You, L. Synchronous crop failures and climate-forced production variability. *Sci. Adv.* **5**, eaaw1976 (2019).
- Chiang, J. C. H. & Sobel, A. H. Tropical tropospheric temperature variations caused by ENSO and their influence on the remote tropical climate. *J. Clim.* **15**, 2616–2631 (2002).
- Oliver, E. C. J. et al. Marine heatwaves. *Annu. Rev. Mar. Sci.* **13**, 313–342 (2021).
- Battisti, D. S. & Hirst, A. C. Interannual variability in a tropical atmosphere–ocean model: Influence of the basic state, ocean geometry and nonlinearity. *J. Atmos. Sci.* **46**, 1687–1712 (1989).
- Wang, C. A review of ENSO theories. *Nat. Sci. Rev.* **5**, 813–825 (2018).
- Harrison, D. & Vecchi, G. A. Westerly wind events in the tropical Pacific, 1986–95. *J. Clim.* **10**, 3131–3156 (1997).
- Vecchi, G. A. & Harrison, D. Tropical Pacific sea surface temperature anomalies, El Niño, and equatorial westerly wind events. *J. Clim.* **13**, 1814–1830 (2000).
- Lian, T., Chen, D., Tang, Y. & Wu, Q. Effects of westerly wind bursts on El Niño: a new perspective: effects of westerly wind bursts on ENSO. *Geophys. Res. Lett.* **41**, 3522–3527 (2014).
- Xie, S.-P. et al. Indian Ocean capacitor effect on Indo–Western Pacific climate during the summer following El Niño. *J. Clim.* **22**, 730–747 (2009).
- Xie, S.-P. et al. Indo-western Pacific ocean capacitor and coherent climate anomalies in post-ENSO summer: a review. *Adv. Atmos. Sci.* **33**, 411–432 (2016).
- Saji, N., Goswami, B., Vinayachandran, P. & Yamagata, T. A dipole mode in the tropical Indian Ocean. *Nature* **401**, 360–363 (1999).
- Le, T., Ha, K.-J. & Bae, D.-H. Causal effects of Indian Ocean dipole on El Niño–Southern Oscillation during 1950–2014 based on high-resolution models and reanalysis data. *Environ. Res. Lett.* **15**, 1040b6 (2020).
- Izumo, T. et al. Influence of the state of the Indian Ocean Dipole on the following year's El Niño. *Nat. Geosci.* **3**, 168–172 (2010).
- Ham, Y.-G., Kug, J.-S., Park, J.-Y. & Jin, F.-F. Sea surface temperature in the north tropical Atlantic as a trigger for El Niño/Southern Oscillation events. *Nat. Geosci.* **6**, 112–116 (2013).
- Ham, Y.-G. & Kug, J.-S. Role of north tropical Atlantic SST on the ENSO simulated using CMIP3 and CMIP5 models. *Clim. Dyn.* **45**, 3103–3117 (2015).
- Park, J.-H., Kug, J.-S., An, S.-I. & Li, T. Role of the western hemisphere warm pool in climate variability over the western North Pacific. *Clim. Dyn.* **53**, 2743–2755 (2019).
- Chen, S. & Wu, R. Impacts of winter NPO on subsequent winter ENSO: sensitivity to the definition of NPO index. *Clim. Dyn.* **50**, 375–389 (2018).
- Chen, S. & Yu, B. The seasonal footprinting mechanism in large ensemble simulations of the second generation Canadian earth system model: uncertainty due to internal climate variability. *Clim. Dyn.* **55**, 2523–2541 (2020).
- Yu, J.-Y. & Kim, S. T. Relationships between extratropical sea level pressure variations and the central Pacific and eastern Pacific types of ENSO. *J. Clim.* **24**, 708–720 (2011).
- Kim, S. T., Yu, J.-Y., Kumar, A. & Wang, H. Examination of the two types of ENSO in the NCEP CFS model and its extratropical associations. *Mon. Weather Rev.* **140**, 1908–1923 (2012).
- Yeh, S.-W., Yi, D.-W., Sung, M.-K. & Kim, Y. H. An eastward shift of the North Pacific Oscillation after the mid-1990s and its relationship with ENSO. *Geophys. Res. Lett.* **45**, 6654–6660 (2018).
- Park, J.-Y., Yeh, S.-W., Kug, J.-S. & Yoon, J. Favorable connections between seasonal footprinting mechanism and El Niño. *Clim. Dyn.* **40**, 1169–1181 (2013).
- Vimont, D. J., Wallace, J. M. & Battisti, D. S. The seasonal footprinting mechanism in the Pacific: implications for ENSO. *J. Clim.* **16**, 2653–2667 (2003).
- Vimont, D. J., Battisti, D. S. & Hirst, A. C. The seasonal footprinting mechanism in the CSIRO general circulation models. *J. Clim.* **16**, 2653–2667 (2003).
- Walker, M. & Bliss, E. World weather V. *Mem. R. Meteorol. Soc.* **4**, 53–84 (1932).
- Rogers, J. C. The North Pacific Oscillation. *J. Climatol.* **1**, 39–57 (1981).
- Linkin, M. E. & Nigam, S. The North Pacific Oscillation–West Pacific teleconnection pattern: mature-phase structure and winter impacts. *J. Clim.* **21**, 1979–1997 (2008).
- Vimont, D. J., Battisti, D. S. & Hirst, A. C. Footprinting: a seasonal connection between the tropics and mid-latitudes. *Geophys. Res. Lett.* **28**, 3923–3926 (2001).
- Alexander, M. A., Vimont, D. J., Chang, P. & Scott, J. D. The impact of extratropical atmospheric variability on ENSO: testing the seasonal footprinting mechanism using coupled model experiments. *J. Clim.* **23**, 2885–2901 (2010).
- Xie, S.-P. & Philander, S. G. H. A coupled ocean–atmosphere model of relevance to the ITCZ in the eastern Pacific. *Tellus Dyn. Meteorol. Oceanogr.* **46**, 340–350 (1994).
- Zhao, J., Kug, J., Park, J. & An, S. Diversity of North Pacific meridional mode and its distinct impacts on El Niño–southern oscillation. *Geophys. Res. Lett.* **47**, e2020GL088993 (2020).
- Chen, S., Yu, B. & Chen, W. An analysis on the physical process of the influence of AO on ENSO. *Clim. Dyn.* **42**, 973–989 (2014).
- Schulte, J. A. & Lee, S. Strengthening North Pacific influences on United States temperature variability. *Sci. Rep.* **7**, 124 (2017).
- Chen, S. & Song, L. Impact of the winter North Pacific Oscillation on the surface air temperature over Eurasia and North America: sensitivity to the index definition. *Adv. Atmos. Sci.* **35**, 702–712 (2018).
- Sung, M.-K. et al. Tropical influence on the North Pacific Oscillation drives winter extremes in North America. *Nat. Clim. Change* **9**, 413–418 (2019).
- Takaya, K. & Nakamura, H. A formulation of a phase-independent wave-activity flux of stationary and migratory quasi-geostrophic eddies on a zonally varying basic flow. *J. Atmos. Sci.* **58**, 608–627 (2001).
- Wang, B. & Xie, X. Low-frequency equatorial waves in vertically sheared zonal flow. Part I: stable waves. *J. Atmos. Sci.* **53**, 449–467 (1996).
- Wang, B. & Xie, X. Low-frequency equatorial waves in vertically sheared zonal flow. Part II: unstable waves. *J. Atmos. Sci.* **53**, 3589–3605 (1996).
- Sooraj, K. P. et al. Effects of the low-frequency zonal wind variation on the high frequency atmospheric variability over the tropics. *Clim. Dyn.* **33**, 495–507 (2009).
- Deser, C. et al. ENSO and Pacific decadal variability in the community climate system model version 4. *J. Clim.* **25**, 2622–2651 (2012).
- Wang, X., Chen, M., Wang, C., Yeh, S.-W. & Tan, W. Evaluation of performance of CMIP5 models in simulating the North Pacific Oscillation and El Niño Modoki. *Clim. Dyn.* **52**, 1383–1394 (2019).
- Park, J.-H. et al. Role of the climatological intertropical convergence zone in the seasonal footprinting mechanism of the El Niño–Southern Oscillation. *J. Clim.* **34**, 5243–5256 (2021).
- Sung, M.-K., Son, S.-W., Yoo, C., Hwang, J. & An, S.-I. Seesawing of winter temperature extremes between East Asia and North America. *J. Clim.* **34**, 4423–4434 (2021).
- Seiki, A. & Takayabu, Y. N. Westerly wind bursts and their relationship with intraseasonal variations and ENSO. Part I: statistics. *Mon. Weather Rev.* **135**, 3325–3345 (2007).

50. Seiki, A. & Takayabu, Y. N. Westerly wind bursts and their relationship with intraseasonal variations and ENSO. Part II: energetics over the Western and Central Pacific. *Mon. Weather Rev.* **135**, 3346–3361 (2007).
51. Kug, J.-S. et al. Simulation of state-dependent high-frequency atmospheric variability associated with ENSO. *Clim. Dyn.* **32**, 635–648 (2009).
52. Sun, M., Li, T. & Chen, L. El Niño phase-dependent high-frequency variability in Western Equatorial Pacific. *Clim. Dyn.* **55**, 2165–2184 (2020).
53. Fu, M. & Tziperman, E. Essential ingredients to the dynamics of westerly wind bursts. *J. Clim.* **32**, 5549–5565 (2019).
54. Gill, A. E. Some simple solutions for heat-induced tropical circulation. *Q. J. R. Meteorol. Soc.* **106**, 447–462 (1980).
55. Sung, M.-K., Son, S.-W., Yoo, C., Hwang, J. & An, S.-I. Dynamics of two distinct subseasonal growth mechanisms of the North Pacific Oscillation. *J. Clim.* **35**, 3141–3156 (2022).
56. Chiang, J. C. H. & Vimont, D. J. Analogous Pacific and Atlantic meridional modes of tropical atmosphere–ocean variability. *J. Clim.* **17**, 4143–4158 (2004).
57. Fan, H., Yang, S., Wang, C., Wu, Y. & Zhang, G. Strengthening amplitude and impact of the Pacific Meridional mode on ENSO in the warming climate depicted by CMIP6 models. *J. Clim.* **35**, 5195–5213 (2022).
58. Di Lorenzo, E. et al. ENSO and meridional modes: a null hypothesis for Pacific climate variability. *Geophys. Res. Lett.* **42**, 9440–9448 (2015).
59. Di Lorenzo, E. et al. North Pacific Gyre Oscillation links ocean climate and ecosystem change. *Geophys. Res. Lett.* **35**, L08607 (2008).
60. Stuecker, M. F. Revisiting the Pacific Meridional Mode. *Sci. Rep.* **8**, 3216 (2018).
61. Kalnay, E. et al. The NCEP/NCAR 40-year reanalysis project. *Bull. Am. Meteorol. Soc.* **77**, 437–471 (1996).
62. Huang, B. et al. Extended reconstructed sea surface temperature, version 5 (ERSSTv5): upgrades, validations, and intercomparisons. *J. Clim.* **30**, 8179–8205 (2017).
63. Sung, M.-K., Yoo, C., Yeh, S.-W., Kosaka, Y. & An, S.-I. Characteristics of the North Pacific Oscillation in CMIP5 models in relation to atmospheric mean states. *J. Clim.* **33**, 3809–3825 (2020).
64. Aru, H., Chen, W. & Chen, S. Is there any improvement in simulation of wintertime Western Pacific teleconnection pattern and associated climate anomalies in CMIP6 comparing with CMIP5 models? *J. Clim.* **35**, 8841–8861 (2021).
65. Chen, H. & Jin, F. Dynamics of ENSO phase–locking and its biases in climate models. *Geophys. Res. Lett.* **49**, e2021GL097603 (2022).

ACKNOWLEDGEMENTS

This research was supported by a National Research Foundation of Korea (NRF) grant funded by the Korean government (MSIT) (NRF-2022R1A3B1077622, NRF-2018R1A5A1024958). Author Sung was supported by KIST institutional grant (Grant

#2E32441). Author J.L. and J.Z. were supported by the National Natural Science Foundation of China (Grant Nos. 42105022, 42088101, and 42030605).

AUTHOR CONTRIBUTIONS

J.Z. compiled the data, conducted analyses, prepared the figures, and wrote the manuscript. M.-K.S. designed the research and wrote the manuscript. All authors discussed the study results and reviewed the manuscript.

COMPETING INTERESTS

The authors declare no competing interests.

ADDITIONAL INFORMATION

Supplementary information The online version contains supplementary material available at <https://doi.org/10.1038/s41612-023-00337-y>.

Correspondence and requests for materials should be addressed to Mi-Kyung Sung or Jong-Seong Kug.

Reprints and permission information is available at <http://www.nature.com/reprints>

Publisher's note Springer Nature remains neutral with regard to jurisdictional claims in published maps and institutional affiliations.



Open Access This article is licensed under a Creative Commons Attribution 4.0 International License, which permits use, sharing, adaptation, distribution and reproduction in any medium or format, as long as you give appropriate credit to the original author(s) and the source, provide a link to the Creative Commons license, and indicate if changes were made. The images or other third party material in this article are included in the article's Creative Commons license, unless indicated otherwise in a credit line to the material. If material is not included in the article's Creative Commons license and your intended use is not permitted by statutory regulation or exceeds the permitted use, you will need to obtain permission directly from the copyright holder. To view a copy of this license, visit <http://creativecommons.org/licenses/by/4.0/>.

© The Author(s) 2023